The Fluid Budget of a Continental Plate Boundary Fault:

Quantification from the Alpine Fault, New Zealand

Catriona D. Menzies[1*], Damon A. H. Teagle[1], Samuel Niedermann[2], Simon C. Cox[3], Dave Craw[4], Martin Zimmer[2], Matthew J. Cooper[1], Jörg Erzinger[2]

[1]*Ocean and Earth Science, National Oceanography Centre Southampton, University of Southampton, SO14 3ZH, UK*

[2]*Helmholtz Centre Potsdam, GFZ German Research Centre for Geosciences, Telegrafenberg, 14473 Potsdam, Germany*

[3]*GNS Science, Private Bag 1930, Dunedin 9054, New Zealand*

[4]*Department of Geology, University of Otago, Dunedin 9016, New Zealand*

*c.menzies@soton.ac.uk

1　**Abstract**

2　　　　Fluids play a key role in modifying the chemical and physical properties of fault zones,

3　which may prime them for repeated rupture by the generation of high pore fluid pressures and

4　precipitation of commonly weak, secondary minerals. Fluid flow paths, sources and fluxes, and

5　the permeability evolution of fault zones throughout their seismic cycles remain poorly

6　constrained, despite their importance to understanding fault zone behaviour. Here we use

7　geochemical tracers of fluid-rock exchange to determine budgets for meteoric, metamorphic

8　and mantle fluids on a major compressional tectonic plate boundary.

9　　　　The Alpine Fault marks the transpressional Pacific-Australian plate boundary through

10　South Island, New Zealand and appears to fail in regular (329±68 years) large earthquakes (M_w

11　~8) with the most recent event in 1717 AD. Significant convergent motion has formed the

12　Southern Alps and elevated geothermal gradients in the hangingwall, which drive crustal fluid

13　flow. Along the Alpine Fault the Alpine Schist of the Pacific Plate is thrust over radiogenic

14　metasedimentary rocks on the Australian plate. The absence of highly radiogenic ($^{87}Sr/^{86}Sr$

15　>0.7200) strontium isotope ratios of hangingwall hot springs and hydrothermal minerals

16　formed at a range of depths in the Alpine Fault damage zone indicates that the fluid flow is

17 restricted to the hangingwall by a cross-fault fluid flow barrier throughout the seismogenic

18 crust. Helium isotope ratios measured in hot springs near to the Alpine Fault (0.15-0.81 R_A)

19 indicate the fault is a crustal-scale feature that acts as a conduit for fluids from the mantle.

20 Rock-exchanged oxygen, but meteoric water-like hydrogen isotope signatures of hydrothermal

21 veins indicate that partially rock-exchanged meteoric fluids dominate down to the top of the

22 brittle to ductile transition zone at ~6 km. Geochemical tracer transport modelling suggests

23 only ~0.02 to 0.05% of total rainfall west of the Main Divide penetrates to depth, yet this

24 recharge flux is sufficient to overwhelm other fluid contributions. Calculated mantle fluid

25 fluxes of CO_2 and H_2O (0.2 and 3 to 13 mol/m^2/yr respectively) and metamorphic H_2O fluxes

26 (4 to 750 mol/m^2/yr) are considerably lower than the focussed meteoric water discharge flux

27 up the Alpine Fault (4 x 10^3 to 7 x 10^4 mol/m^2/yr), driven by the >3000 m hydrologic head of

28 the Southern Alps. Meteoric waters are primarily responsible for modifying fault zone

29 permeability during fluid-rock interactions and may facilitate the generation of high pore fluid

30 pressures that could assist episodic earthquake rupture.

31 **1. Introduction**

32   Despite the importance of fluids in the evolution of faults throughout their seismic

33 cycles by controlling heat and chemical transport (Blanpied et al., 1992) and influencing fault

34 failure mechanics (Sibson, 1992), there are few observations that quantify the fluid origins,

35 fluxes, and flow paths on active fault zones. Conceptual models suggest that fault zone

36 permeability is dynamic, evolving from highly permeable, directly post rupture, to effectively

37 sealed by the deposition of secondary minerals in pore spaces due to earthquake-related pulses

38 of fluid (Byerlee, 1993) and compaction of fault gouge (Blanpied et al., 1992; Sleep and

39 Blanpied, 1992). Fluids may facilitate earthquake nucleation when elevated pore fluid

40 pressures reduce the effective normal stress, and previous studies have predicted that large

41 faults require high pore fluid pressures to explain fault zone weakness and episodic earthquake

rupture (Blanpied et al., 1992; Rice, 1992). Using assumed hydrological conditions, modelling

has provided estimates of fluid fluxes and flow rates required to maintain overpressure in near-

vertical strike slip faults (e.g. Faulkner and Rutter (2001)), and identified possible fluid sources;

mantle fluids (Fulton and Saffer, 2009; Kennedy et al., 1997; Rice, 1992); metamorphic fluids

(Fulton et al., 2009); meteoric fluids (Blanpied et al., 1992; Byerlee, 1993; O'Neil, 1984).

However, the relative contributions of different fluid sources have not been constrained by

direct observations for a plate boundary fault zone. Here we apply geochemical tracers of fluid-

rock interaction to the unique geometry of the Alpine Fault, New Zealand, to develop the first

fully integrated fluid budget and to quantify fluid sources, fluxes, and flow paths of a major

continental fault zone.

1.1. Geological setting

The Alpine Fault is the transpressional Pacific-Australian plate boundary through the

South Island, New Zealand that accommodates the majority of the relative strike slip motion

(~23-25 mm/yr, Norris and Cooper (2007)). To accommodate ~10 mm/yr plate convergence,

the Alpine Fault dips at ~45° to the south east and has dip-slip rates of 10 mm/yr, locally up to

>12 mm/yr (Norris and Cooper, 2007). This geometry has formed the >3000 m high Southern

Alps. Because the Alpine Fault has uplifted its ~1 km wide damage zone, surface outcrops and

shallow boreholes provide a unique profile of deformation and fluid flow through a complete

crustal section (Fig. 1) (Norris and Cooper, 2007). The low elevation Australian Plate footwall

is composed of Palaeozoic metasediments and minor (<5%) Palaeozoic to Mesozoic granitoids

(Cox and Sutherland, 2007). These rocks are juxtaposed by the Alpine Fault against

hangingwall Pacific Plate quartzofeldspathic late Paleozoic to early Mesozoic metasediments,

with minor metabasalt, metamorphosed into amphibolite-facies Alpine Schist.

The Alpine Fault fails in regular large earthquakes (~M_w7 to 8) (Sutherland et al., 2007)

and is late in its 329±68 year seismic cycle, having last ruptured in 1717 AD (Berryman et al.,

67   2012). Rapid uplift caused by ca. 10 mm/yr Alpine Fault dip slip (Norris and Cooper, 2007)

68   and very high erosion rates in the Southern Alps have elevated geothermal gradients and the

69   base of the brittle to ductile transition zone (BDTZ) in the hangingwall (Koons, 1987), resulting

70   in a relatively thin seismogenic crust (8-10 km) (Boese et al., 2012). The high topography and

71   geothermal gradient drive meteoric fluid flow (Menzies et al., 2014). This has resulted in warm

72   springs hosted by the Alpine Schist up to 17 km east of the fault (Fig. 1a) and the deposition

73   of quartz, chlorite, adularia, calcite, and gold-bearing veins from the near-surface down to the

74   BDTZ (Menzies et al., 2014). Regions of low resivitivy and seismic velocity imaged in the

75   middle crust have been interpreted to be zones of metamorphic dehydration (Fig. 1;

76   Wannamaker et al. (2002)).

77   At shallow levels the Alpine Fault has a <0.5 m-thick clay-rich principal slip zone and

78   the related damage zone is predominantly developed in the hangingwall from the mylonitic

79   Alpine Schist. This damage zone comprises 10 to ~60 m of strongly hydrothermally altered

80   cataclasites and breccias with common fractures filled by calcite and clay minerals (Norris and

81   Cooper, 2007; Schleicher et al., 2015; Toy et al., 2015; Warr and Cox, 2001). Shallow drilling

82   across the Alpine Fault in the ~150 m deep DFDP-1b borehole measured a 0.53 MPa fluid

83   overpressure from the hangingwall to the footwall, indicating the principal slip zone is

84   impermeable to cross-fault fluid flow in the near-surface (Sutherland et al., 2012). This is in

85   agreement with laboratory measurements of low permeability in Alpine Fault gouges (10^{-20}

86   m^2) and cataclasites (10^{-15}-10^{-18} m^2) (Boulton et al., 2012; Carpenter et al., 2014).

87   **2. Methods**

88   **2.1. Spring water sampling**

89   Spring water samples for $\delta^{13}C_{DIC}$ determinations were collected in new 1 L or 60 mL,

90   acid-cleaned HDPE bottles with minimal headspace, then sealed with parafilm tape. Samples

91   for trace element analysis were filtered through 0.2 μm filter paper and acidified (with 1 mL/L

92 quartz distilled concentrated HNO_3). Very heavy rainfall events can impact the local

93 geothermal systems (Cox et al., 2015) and sampling during such events was avoided. Alkalinity

94 was determined in the field by titration with 0.1 N HNO_3. Total alkalinity was calculated using

95 the Gran Function Plot method.

96 For gas geochemistry analyses, spring waters were sampled in copper tubes sealed by

97 steel clamps. These samples were not acidified or filtered because these processes promote

98 degassing and therefore fractionation of the isotopes between dissolved and gaseous phases. In

99 addition, at four locations free gas bubbling through water pools was sampled directly in glass

100 flasks after filling them with spring water and replacing the water with gas. To identify if

101 interaction with organic particulate material occurred after sampling we compare $\delta^{13}C$ values

102 for degassed water samples and gas samples. All of which are slightly lower in the gas samples

103 indicating that no interaction with organic material post sampling occurred in these samples

104 (see Supplementary Materials Tables S1).

105 **2.2. $^{87}Sr/^{86}Sr$ and Sr concentration measurements**

106 Spring waters and hydrothermal calcite veins were prepared and measured using the

107 Isotope Geochemistry class 100 clean laboratory suite at the University of Southampton.

108 *Hydrothermal calcite dissolution*

109 For each sample 10-20 mg of pure calcite was handpicked from a crushed mineral vein. The

110 mineral separates were then sonicated in Milli-Q water (18.2 MΩ H_2O), dried and hand crushed

111 using an agate mortar and pestle. ~10 mg of sample was then dissolved in 0.5 M analytical

112 grade or ROMIL sub-boiled acetic acid.

113 *Determination of strontium concentrations*

114 Dissolved calcite samples and spring waters were analysed for strontium concentrations using

115 a PerkinElmer Optima 4300 DV ICP-OES. Samples were appropriately diluted with 2% sub

116 boiled HNO_3, as were synthetic multi-element standards used to calibrate the instrument.

117 Precision and accuracy were assessed using international reference solution SLRS4 and in-

118 house reference material Sco2/15. Precision was better than 2.8%, accuracy better than 8%,

119 and detection limits were 0.05 ppb for these measurements.

120   *$^{87}Sr/^{86}Sr$ determination*

121 Strontium was separated from dissolved whole rocks, calcite and spring waters using Sr-spec

122 resin following Harris et al. (2015). Over the course of the study strontium isotopes were

123 measured on two VG Sector 54 Thermal Ionisation Mass Spectrometers (TIMS) and a

124 ThermoFisher Scientific TritonPlus TIMS. Precision and accuracy were assessed using

125 international reference material NBS987. The average values for $^{87}Sr/^{86}Sr$ of NBS987 on the

126 three instruments were 0.710241 ± 0.000027 (2σ, n=70) and, 0.710241 ± 0.000019 (2σ, n=71)

127 for the two VG Sector 54 instruments and 0.710244 ± 0.000019 (2σ, n=135) for the Triton

128 Plus. Internal precision was monitored by measuring 150 ratios for each sample and calculating

129 2 standard errors of these measurements (standard errors are reported in Tables S3 and S4).

130 Strontium column blanks were <10 pg.

131 **2.3. Gas geochemistry**

132   At GFZ Potsdam, chemical compositions of free gas samples were determined using an

133 Omnistar (Pfeiffer Vacuum) quadrupole mass spectrometer and then appropriate volume splits

134 were analysed for noble gas concentrations and isotopic compositions following Niedermann

135 et al. (1997). Measured $^{3}He/^{4}He$ ratios and ^{4}He concentrations were corrected for air

136 contamination based on ^{20}Ne following the method of Giggenbach et al. (1993).

137   Analyses of the total gas composition were performed using an Omnistar quadrupole

138 mass spectrometer with a closed ion source, a mass range of 1 to 100 amu and a heated and

139 temperature-regulated gas inlet system. The gas was transferred into the mass spectrometer

140 with a flow rate of 1-2 cm^3/min. at ~5×10^{-6} mbar pressure and analyzed for H_2, He, CH_4, O_2,

141 N_2, Ar, and CO_2. Calibration of the mass spectrometer was performed with certificated test

142   gases at the same pressure conditions. The relative standard deviation (2σ, n = 10) of air

143   components was <10%.

2.4. $\delta^{13}C$ determinations

145   *Calcite*

146   Microscopically interrogated, hand-picked, clean calcite was crushed with an agate mortar and

147   pestle to provide ~1 mg of calcite powder. Analysis was carried out on the Europa GEO 20-20

148   mass spectrometer with a CAPS preparation system at the University of Southampton. Standard

149   external analytical precision based on replicated analysis of in-house standards calibrated to

150   NBS-19 is better than 0.1 ‰.

151   *Dissolved inorganic carbon*

152   Carbon isotope values of spring waters and total dissolved inorganic carbon (TDIC) were

153   determined at the National Isotope Centre, GNS Science, New Zealand between 2009 and

154   2012. Water samples were reacted with 85% phosphoric acid, the resulting CO_2 extracted and

155   purified to run in duel inlet mode on a Europa GEO 20-20 mass spectrometer. A sodium

156   bicarbonate standard solution was analysed to check the extraction procedure. Carbonate

157   content was calculated from the measured CO_2 pressures in milligrams of carbonate per

158   kilogram of water. The $\delta^{13}C$ values are reported with respect to VPDB. Reported errors

159   combine the statistical errors from sample and standard determinations, combined in

160   quadrature with a system error component based on the analysis of an ongoing series of

161   measurements on an oxalic acid standard.

3. Results

3.1. Strontium isotopes - fluid flow paths

164   The Alpine Fault juxtaposes isotopically distinct rocks. The footwall metasediments and minor

165   (<5%, see Fig. 1) intrusive granitoids have high $^{87}Sr/^{86}Sr$ ratios (Buller Terrane metasediments

166    $^{87}Sr/^{86}Sr$ = 0.7239-1.0018; Adams (2004); Pickett and Wasserburg (1989); Tulloch et al.

167 (2009); Table 1, Table S6). In contrast, the hangingwall Alpine Schist yield a narrow range of

168 relatively low $^{87}Sr/^{86}Sr$ ratios ($^{87}Sr/^{86}Sr$ = 0.7039-0.7137, average = 0.7091±0.0019 (1σ), n =

169 45, including data from Adams et al., 2009; Adams and Graham, 1997; Horton et al., 2003)

170 (Table 1, Table S6, Fig. 2). As the host rocks either side of the Alpine Fault have similar

171 strontium concentrations, we would expect comparable strontium concentrations in fluids

172 associated with these rock types, but $^{87}Sr/^{86}Sr$ ratios would be significantly more radiogenic in

173 the footwall. We have measured $^{87}Sr/^{86}Sr$ of warm springs and hangingwall hydrothermal

174 calcites to ascertain fluid flow paths. The $^{87}Sr/^{86}Sr$ ratios of spring waters (0.7084-0.7113, n =

175 13, Table S4), fault zone calcite veins formed throughout the fault zone from ductile to brittle

176 conditions, and near-surface cataclasite and fault gouge cements (0.7041-0.7114, n = 62, Table

177 S3) are all within range of hangingwall Alpine Schist host rocks (Fig. 2).

178 Fluid and vein mineral $^{87}Sr/^{86}Sr$ ratios subtly decrease with proximity to the Alpine

179 Fault due an increased proportion (with proximity to the plate boundary) of metabasic rocks

180 with lower $^{87}Sr/^{86}Sr$ ratios in the Alpine Schist mylonites (Cox and Sutherland, 2007). There is

181 no evidence that fluids circulating and mineralising in the hangingwall have interacted with

182 radiogenic Sr-bearing rocks of the footwall Australian Plate (Fig. 2). This indicates there has

183 been no cross-fault fluid flow from the footwall to the hangingwall and suggests that

184 hangingwall fluids are isolated from the footwall at depth. Further, the warm springs upwell

185 above the Alpine Fault zone, not within it. There are no thermal springs in the footwall of our

186 study area, and footwall cataclasites are less altered than those in the hangingwall (Toy et al.,

187 2015). These observations together with low Alpine Schist-like strontium isotope ratios

188 indicate that the Alpine Fault is a hydrologic barrier to cross-fault flow throughout the

189 seismogenic crust.

190 **3.2. Warm spring gas chemistry**

Springs in the hangingwall of the Alpine Fault have discernible mantle He contributions, with $^3He/^4He$ >0.1 R_A (0.15-0.81 R_A, Fig. 3a, Tables S1, S2; R_A is the atmospheric $^3He/^4He$ ratio of 1.39×10^{-6}). Springs further from the fault have significantly lower $^3He/^4He$ signatures, indicative of crustal ^4He production (0.018-0.030 R_A) only, with no resolvable mantle contribution (Fig. 3a). These springs also have the highest ^4He concentrations (Fig. 3d), up to two orders of magnitude greater than those adjacent to the Alpine Fault. Given the uniformity of the host Alpine Schist this indicates that these spring waters have had longer transit times or flow paths and therefore have been subjected to a greater crustal production of ^4He by radioactive decay of uranium and thorium in the rock mass.

Warm springs contain abundant dissolved CO_2 (1-18 mmol/kg), and some springs effervesce CO_2 at the surface. Bicarbonate to calcium molar ratios of 7-19 in springs are considerably higher than can be accounted for through calcite dissolution (HCO_3^-/Ca^{2+} from 1-2), requiring an additional CO_2 source. Warm springs that have a contribution of mantle He have higher CO_2 concentrations than those with crustal $^3He/^4He$ signatures (4.1-18.4 mmol/kg, versus 1.0-3.0 mmol/kg, Fig. 3b, Table S1). These springs also have the highest carbon isotope ratios ($\delta^{13}C_{CO2}$ = -11.6 to -6.7 ‰ versus -16.8 to -12.3 ‰; Barnes et al. (1978); Fig. 3c, Table S1 and S2). Most near-surface calcite cements in Alpine Fault cataclasites and gouges, and hydrothermal calcite veins yield calculated fluid $\delta^{13}C$ values within the crustal/ mantle range (-13.8 to -3.8 ‰, average -6.6±1.7, n = 59, Table S5).

4. Discussion

4.1. Fluid budgets on the Alpine Fault

Although the Southern Alps are a major orogenic belt with rapid rates of uplift, there is no evidence for current magmatic activity in the Alpine Fault region. Consequently our potential fluid sources are limited to meteoric waters, fluids generated by metamorphic dehydration reactions, and mantle fluids. To estimate the fluxes of our different end member

216   fluids up the Alpine Fault we use our geochemical measurements to quantify the relative

217   contributions of these different fluid sources.

218   **4.1.2. Calculating the mantle fluid flux**

219   There is a mantle contribution of up to 10% He in geothermal waters near to the Alpine

220   Fault, indicating the fault is a conduit for mantle-derived fluids into the upper crust, similar to

221   other crustal-scale fault zones. A minimum upward flow rate of mantle He (q), which is the

222   minimum rate at which a mantle fluid must move through the crust to overcome the crustal

223   production of ^{4}He and retain the measured ^{3}He/^{4}He ratio, can be calculated following eq. 1

224   (Kennedy et al., 1997; Kulongoski et al., 2013):

225    $$q = \frac{h_{crust}\, \rho_r\, P_{He}}{\rho_f\, [^4He]f,m} \times \left[\frac{R_s - R_c}{R_m - R_s}\right] \qquad (eq.\ 1)$$

226   Where h_{crust} is crustal thickness; ρ_f and ρ_r are fluid and solid densities respectively; $P_{(He)}$ is the

227   ^{4}He solution rate (cm^{3}STP/g H$_2$O/yr), based on the production rate of ^{4}He, rock density, and

228   the fractional effective porosity; $[^4He]_{f,m}$ is the original mantle fluid ^{4}He concentration; and $R_{c,}$

229   R_m and R_s are the ^{3}He/^{4}He ratios in the crust, mantle and sample respectively. The key

230   parameters determined in this study are: the calculated original mantle fluid ^{4}He concentrations

231   ($[^4He]_{f,m}$), and the measured sample ^{3}He/^{4}He ratios (R_s) and ^{4}He concentrations ($[He_s]$, eq. 2).

232   Reasonable values for other parameters are estimated from published data: crustal thickness

233   (h_{crust}), the crustal ^{4}He production rate ($P_{(He)}$) based on host rock concentrations of U and Th

234   (see Table 2), ^{3}He/^{4}He ratios of crust (R_c) and mantle (R_m), and fluid and solid densities (ρ_f, ρ_r).

235   Calculated mantle fluid flow rates for the Alpine Fault are between 0.42 and 2.6 m/yr. These

236   rates are significantly higher than estimated for the San Andreas Fault (0.004-0.14 m/yr;

237   Kennedy et al. (1997); Kulongoski et al. (2013)), the North Anatolian Fault (~0.13 to 0.19

238   m/yr; de Leeuw et al. (2010)) and the Karakoram Fault (~0.012-0.019 m/yr; Klemperer et al.

239   (2013)).

240   These minimum mantle flow rates can be converted into ^{3}He fluxes:

241    $^3He\ flux = q \times \rho_f \times [He_s] \times R_s$ *(eq. 2; Kulongoski et al. (2013))*

242   This yields ^{3}He fluxes of 2 x 10^{-11} to 9 x 10^{-11} mol/m^2/yr. These calculated mantle helium fluxes

243   can be combined with a mantle fluid CO_2/^{3}He ratio of 2x10^9 (Marty and Jambon, 1987) and a

244   H_2O/^{3}He ratio of 3x10^{10}-1x10^{11} (Hilton and Porcelli, 2003) to convert ^{3}He fluxes to CO_2 and

245   H_2O fluxes. Using the spring with the highest ^{3}He/^{4}He ratio (Amythest spring), indicating least

246   dilution by crustal ^{4}He, and these mantle CO_2/^{3}He and H_2O/^{3}He ratios, a CO_2 flux of 0.18

247   mol/m^2/yr and a H_2O flux of 2.5 to 12.7 mol/m^2/yr is calculated for a conduit up the Alpine

248   Fault from the mantle (Table 2). Flow rates and fluxes calculated using other springs are

249   outlined in the Supplementary Materials Tables S1 and S2, all springs that contain a mantle

250   component have similar order of magnitude fluxes. These calculations rely on a number of

251   parameters from published data, and those with the greatest influence on our results are the

252   mantle CO_2/^{3}He and H_2O/^{3}He ratios, and the crustal production rate of ^{4}He. Changes in these

253   values by 10% results in a 10% change in the fluxes calculated. The mantle CO_2/^{3}He ratio used

254   has been shown to be a robust estimate for the mantle component in gases in a range of

255   geodynamic settings (Marty and Jambon, 1987). The mantle H_2O/^{3}He ratio is more poorly

256   constrained, and hence we use a range spanning an order of magnitude in our calculations.

257   Crustal production rates are based on the U and Th concentrations measured in the host rocks.

258   The ^{4}He solution rate is controlled by the fractional effective porosity of the system which is

259   estimated as a maximum of 0.1 (for the uppermost crust where sampled spring waters

260   circulate); if this value is halved, then the resulting flux estimates double owing to an increased

261   ^{4}He solution rate.

262   Mantle fluids are reported in numerous fault-controlled, seismically active settings

263   across New Zealand (Giggenbach et al., 1993). Seismicity in the mantle down dip of the Alpine

264   Fault (Lamb et al., 2015), below the schematic lower-crustal décollement (Fig. 1b), may

265   indicate the flow path for fluids from the mantle to the Alpine Fault conduit and up to the

266   surface.

267   Boiling during the decompression path of these fluids may affect the $CO_2/^3He$ ratios

268   and isotopic values, leading to decoupling of the isotopic tracers we use to investigate the

269   mantle fluid flux. Boiling textures in the Inboard and Main Divide Zones of the Southern Alps

270   indicate there has been immiscibility during the fluid flow history, as discussed in detail by

271   Jenkin et al. (1994). Our primary data for the estimates of the mantle fluid flux are fluid and

272   gas $^3He/^4He$ ratios. If these fluids have boiled, this generates fluids with lower R/R_A values and

273   gases with higher R/R_A values as ^3He is preferentially lost to the gas phase. If this gas phase

274   is redissolved in shallower level fluids the R/R_A value of the resulting fluid would be higher,

275   leading to larger estimates of the mantle fluid flux. However, when $CO_2/^3He$ and R/R_A values

276   are available for both fluid and gas for the same spring these are similar (see Supplementary

277   Materials Tables S1 and S2). Also the variability in R/R_A values of springs along strike adjacent

278   to the Alpine Fault is minor (0.64-0.81; Supplementary Materials Tables S1 and S2) suggesting

279   that although our estimates for mantle flow rates are maxima, we consider them to be close to

280   the true value.

281   **4.1.3. Calculating the metamorphic fluid flux**

282   The rapid convergence of the Pacific and Australian plates in the Southern Alps region

283   and the strong climate asymmetry caused by the orographic barrier of the Southern Alps leads

284   to crustal thickening and the rapid movement of mid-crustal rocks through this orogen (Koons,

285   1990). The prograde metamorphism of greenschist facies Otago Schist to amphibolite facies

286   Alpine Schist results in a change in the volatile content (*ΔLOI*) of ~1 wt.% (Pitcairn et al.,

287   2014). This value can be combined with the thickness of rock undergoing dehydration (*T*) and

288   the plate convergence rate (*CR*) to estimate a metamorphic fluid flux. In the crustal root of the

289   Southern Alps a ~5 km thickness of rock is currently undergoing metamorphism to amphibolite

facies (Pitcairn et al., 2014) and the plate convergence rate is ~0.01 m/yr (Norris and Cooper,

2007). We can calculate how much water is released from a 1 km strike length of the orogen

in a year following:

Production of H_2O/ year = $\Delta LOI \times CR \times T \times L \times \rho_r$ (*eq.3*)

where L is the strike length and ρ_r is the rock density. Using reasonable values for rock density

(Table 2), 8×10^7 mol/year of H_2O per 1 km strike length would be liberated from the

dehydrating root. The production rate is directly proportional to the thickness of the

dehydrating root, the loss of volatiles during metamorphic dehydration reactions, and the

convergence rate, all of which are well constrained in this system. Here we approximate the

change in volatile content during metamorphism to amphibolite facies to be due to the loss of

H_2O, although in reality CO_2 and other volatiles are also lost. Fluid inclusions in veins in the

Inboard Southern Alps, but away from the Alpine Fault Zone have ~5 mol.% CO_2 (Craw and

Norris, 1993). Using this measurement the annual metamorphic CO_2 production is estimated

to be ~4×10^6 mol/year per kilometre of orogen. Our calculations provide a long time scale

estimate of metamorphic fluid production based on the plate convergence rates with a caveat

that the instantaneous release rates may be episodically higher or lower than these estimates.

In order to compare this with our estimate of mantle fluid we must consider the area

that this discharge flux is distributed over in three scenarios where all the metamorphic fluid is

focused up: (1) a 100 m to 1000 m wide Alpine Fault Zone; (2) the 2 km wide area imaged as

a conductive zone in the SIGHT survey, interpreted as metamorphic waters at depth

(Wannamaker et al. (2002); Fig. 1); and (3) assuming that upwelling metamorphic fluids are

not focused but distributed over the entire area of the Inboard Zone from the Alpine Fault to

the Main Divide of the Southern Alps (shown on Fig. 1b). The maximum metamorphic fluid

flux estimate is 750 mol/m^2/yr up a 100 m wide Alpine Fault zone and the minimum is 4

mol/m^2/yr across the entire Inboard Zone of the Southern Alps (Table 3). 5% of this output flux

is composed of metamorphic CO_2, and the minimum output CO_2 flux estimate is similar to the mantle CO_2 flux (Table 3). However, hydrogen isotope measurements of quartz and chlorite veins throughout the Alpine Fault zone yield strong meteoric water signatures with no requirement for a metamorphic fluid contribution to the mineralizing fluids, and indicating that meteoric water fluid fluxes are orders of magnitude larger than the potential metamorphic fluid flux (Menzies et al., 2014).

4.1.4. Calculating the meteoric water fluid flux

The Southern Alps experience exceptionally high rainfall, locally exceeding 10 m/yr, but the infiltration rate of this rainfall deep into the mountains is poorly constrained. Infiltration rates of between 0.3 and 20% are estimated for shallow level penetration (10-100s of metres) of rainfall into the ridges of the Inboard Zone (Sims et al., 2015). Here we use relative tracer transport distances of O and H and the isotopic compositions of deeply formed quartz veins (6-8 km) to calculate likely proportions of rainfall that may reach mid-crustal levels and to estimate meteoric water fluid fluxes up the Alpine Fault.

Water circulating in the upper 2 km of the crust at temperatures <200 °C retains meteoric δD and $\delta^{18}O$ values (Menzies et al., 2014). Below 2 km, waters become partially equilibrated with rock and by the top of the BDTZ at ~6 km depth $\delta^{18}O$ values are equilibrated with the rocks, but δD values of deeply formed quartz veins still indicate formation from meteoric water (Menzies et al., 2014). These observations provide information on the relative tracer transport distances of the oxygen and deuterium meteoric water signature, which can be used to calculate the time-integrated fluid flux for this system (Bickle and McKenzie, 1987).

Firstly we estimate meteoric fluid fluxes using measured isotopic values of partially deformed vein minerals and fluid inclusions (Menzies et al., 2014). From mass balance, assuming the equilibrium fluid-rock tracer exchange for oxygen and hydrogen, the minimum transport distance (*h*) of a specific tracer is a function of the time integrated fluid flux (*Σflux*)

340 and the solid/fluid partition coefficient (K_d), following equation 4 (Bickle and McKenzie,

341 1987):

342 $h = \Sigma flux/((\rho_s K_d)/\rho_f)$ *(eq. 4)*

343 The assumption of equilibrium fluid-rock tracer exchange is reasonable because fluid

344 movement in the system of interest, below the active meteoric-dominated regime that feeds hot

345 springs, is probably along grain boundaries, at elevated temperatures (>200 °C), and in fine-

346 grained rocks, all factors that favouring equilibrium isotopic exchange. Transport distances

347 evaluated by isotopic measurements show that the fluid oxygen isotope values are rock

348 dominated after a short flow distance (on the order of hundreds of metres) and fluid hydrogen

349 isotope values remain meteoric-like at 6 km depth (4 km along the flow path). Using these

350 distances we can estimate a time integrated fluid flux for this system. For tracer transport

351 distances of ~120 and 4000 m, and ~300 and 10,000 m for oxygen and hydrogen respectively

352 we estimate time integrated fluid fluxes between ~200 and ~500 m (m^3/m^2; equivalent to 1 x

353 10^7 to 2.6 x 10^7 moles/m^2) (Table 4). Note, that because groundwater strontium concentrations

354 are low (0.1-21 mmol/L, Cox et al. (2015)) fluids become rock-dominated at very small

355 transport distances (2 x 10^{-3} to 1 m) for these time integrated fluid fluxes. As the hydrogen

356 isotope values remain meteoric-like, with only minor rock influence, the transport distance

357 must be greater than 4 km, implying that our estimated integrated fluid flux of 200 m is a

358 minimum.

359   Secondly, we consider a column of rock of 4 x 1 x 1 km to estimate likely fluid fluxes

360 as constrained by measured $\delta^{18}O$ and δD values of fluids in the middle crust. For reasonable

361 values of crustal permeability between ~2 and 6 km depth (k = 1 x 10^{-15} to 1 x 10^{-17} m^2; Manning

362 and Ingebritsen (1999)), fluid viscosity (μ = 2 x 10^{-4} kg/m/s), fluid density at higher

363 temperatures and pressures (ρ_f = 0.9 g/cm^3), and acceleration due to gravity (g = 9.8 m/s^2), we

364 can estimate a hydraulic conductivity (K, m/s, Table 4) following:

365 $K = (k \times \rho_f \times g) / \mu$ (eq. 5)

366 Using hydraulic conductivity and the head gradient (height, y/ length, x; *3000 m/ 20,000 m*) of

367 the orogen we can estimate the Darcy velocity (Q/A, Table 4) in $m^3/m^2/s$ following:

368 $Q/A = K \times (y / x)$ (eq.6)

369 To calculate a fluid flux for the system we estimate the mass of water passing through the 4 x

370 1 x 1 km column following equation 7, over a reasonable time period following:

371 *Mass $H_2O = Q/A \times t \times \rho_f$*   (eq. 7)

372 To match the fluid fluxes calculated from tracer transport modelling above, permeabilities

373 towards the lower end of those commonly estimated for the middle crust, or times shorter than

374 100,00 years are required. For hydrogen transport distances of 4000 to 10,000 m permeabilities

375 of 1 x 10^{-17} m^2 to 2.5 x 10^{-17} m^2 and 100,000 years or 1 x 10^{-16} m^2 to 2.5 x 10^{-16} m^2 and 10,000

376 years are required to maintain the time-integrated fluid flux of ~1.1 x 10^7 to 2.7 x 10^7 moles of

377 water (Table 4). In agreement with our tracer transport calculations we prefer higher fluid flux

378 estimates that give greater tracer transport distances. These may be obtained with a marginally

379 higher minimum permeability (1.5 x 10^{-17} m^2 or 1.5 x 10^{-16} m^2 over 100,000 and 10,000 years

380 respectively) which would give hydrogen tracer transport distances of ~6000 m and a revised

381 minimum fluid flux of 160 mol/m^2/yr (100,000 years) or 1600 mol/m^2/yr (10,000 years) (Table

382 4). Measurements of mean fluid residence times are required to fully constrain fluid flow in

383 these systems, but here we prefer the longer, more reasonable time of 100,000 years. Therefore

384 tracer transport modelling indicates an input flux of meteoric waters to deeper crustal levels,

385 under reasonable crustal permeability conditions is between ~160 and 250 mol/m^2/yr. This is

386 equivalent to ~0.02 to 0.05% of rain falling at the surface being transported to ~6 km depth,

387 between one and three orders of magnitude lower than estimates of near-surface infiltration

388 rates (Sims et al., 2015).

389   Strongly altered Alpine Fault rocks with a high proportion of clay and carbonate

390   minerals (Sutherland et al., 2012; Toy et al., 2015) indicate the Alpine Fault zone has

391   experienced higher fluxes of water and CO_2 than the adjacent crust where there is little evidence

392   for retrogression of the metamorphic amphibolite facies mineral assemblages. $^3He/^4He$ ratios

393   indicate that the Alpine Fault is a conduit for mantle fluids throughout the crust and strontium

394   ratios preclude large scale fluid movement from footwall to the hangingwall. This combination

395   of up-fault conduit and across-fault fluid-flow barrier indicates the development of a structure

396   that focuses the flow of deeply infiltrating meteoric fluids driven by the topographic head of

397   the >3000 m Southern Alps that channels upwelling meteoric fluids back towards the surface.

398   Using our estimated input fluxes, which are constrained using tracer transport distances

399   estimated from isotopic measurements of fluids at depth, we can estimate fluxes on the Alpine

400   Fault zone assuming focusing of fluid up different fault areas. Using the same scenarios as for

401   the metamorphic fluid estimates (Table 3) these yield maximum fluid fluxes up a 100 m to

402   1000 m wide fault zone of 2×10^4 to 4×10^4 mol/m^2/yr and 2×10^3 to 4×10^3 mol/m^2/yr

403   respectively, and a minimum fluid flux, assuming no focussing up the fault with outflow

404   dispersed over the Inboard Zone, of 120 mol/m^2/yr. Due to the geometry of the orogen, where

405   hydraulic gradients focus fluid flow away from the Main Divide towards the impermeable

406   barrier of the Alpine Fault, and the strong alteration of Alpine Fault zone rocks, we consider

407   the focussed estimates most reasonable.

408   **4.2. The balance between fluid sources in the Alpine Fault Zone**

409   Hydrogen isotopic data indicates that only meteoric waters are detectable down to

410   middle crustal levels in the Southern Alps (Jenkin et al., 1994; Menzies et al., 2014). If the

411   meteoric water infiltration flux is discharged on the Alpine Fault whereas metamorphic waters

412   regionally leak out throughout the Inboard Zone (Table 3), the meteoric water flux is two to

413   three orders of magnitude higher than the metamorphic flux. In contrast, if metamorphic and

17

414 meteoric waters are focussed over the same area, the meteoric water flux remains significantly

415 higher than the metamorphic flux, by an order of magnitude. Studies of the San Andreas Fault

416 suggest that it is difficult to focus metamorphic fluids derived by regional metamorphic

417 processes into zones of high fluid pressure on a near vertical fault (Fulton et al., 2009).

418 However, the Alpine Fault dips at ~45-50° and is projected to flatten at depth to intersect a

419 conductive, seismic low velocity zone at ~20 km (Fig. 1b), considered to be a metamorphic

420 fluid production zone (Wannamaker et al., 2002). Therefore it is possible that metamorphic-

421 derived fluids may be channelled up the Alpine Fault. Alternatively they may regionally leak

422 out over the Inboard Zone, evidenced by late stage vein mineralisation throughout the Alps.

423 Either way, the meteoric water flux is at least one order of magnitude higher than the

424 metamorphic flux. ^{3}He/^{4}He data indicates that mantle fluids move up the Alpine Fault from the

425 mantle to the near-surface. However, if estimated mantle fluid fluxes are compared with our

426 estimated meteoric water fluxes over any area, they are at least four times to an order of

427 magnitude lower than meteoric waters (Table 2).

428 **4.3. Fluid focussing**

429 Strontium isotope data indicates that fluid flow in the Southern Alps orogen is restricted

430 to the hangingwall of the fault and a low permeability cross-fault fluid flow barrier exists in

431 the plane of the fault throughout the seismogenic crust. The damage zone of the Alpine Fault

432 consists of a low permeability principal slip zone (PSZ) surrounded by a highly fractured,

433 partially sealed, more permeable zone 10 to ~60 m wide (Sutherland et al., 2012). In the

434 hangingwall this damage zone is overprinted by an "alteration zone" where intense fluid-rock

435 reactions have occurred, altering primary amphibolite facies minerals to clay minerals and

436 carbonate (Sutherland et al., 2012; Toy et al., 2015). This zone of alteration, as well as mantle

437 ^{3}He/^{4}He signatures in springs near to the Alpine Fault, provide evidence for the focussing of

438 fluid flow through a small volume of rock in the hangingwall of the Alpine Fault zone that

439   provides a conduit from the mantle to the near surface. Laboratory permeability measurements

440   of fault rocks from the Nojima fault zone, Japan (Lockner et al., 2009) show that although the

441   PSZ gouge has very low matrix permeability, the damage zone surrounding the PSZ has higher

442   matrix permeability than the rocks outside the fault zone, and therefore has the capacity to

443   channel fluids up the fault zone, whereas the low permeability PSZ gouge acts as a barrier to

444   cross fault fluid flow (Lockner et al., 2009). This situation is comparable to the Alpine Fault

445   zone, where a low permeability PSZ must extend throughout the seismogenic crust, as

446   evidenced by strontium isotope ratios of vein minerals, and above this the hangingwall damage

447   zone has been altered by fluids that have been channelled up the fault zone.

448   Taking this into consideration, we infer that the regional meteoric water recharge flux

449   is concentrated onto a 100 to 1000 m wide fault discharge zone. We therefore present a

450   meteoric fluid flux on the Alpine Fault of 2×10^3 to 4×10^4 mol/m^2/yr, accounting for >99%

451   of the fluid flowing through the Alpine Fault zone, if the metamorphic fluid flux is predicted

452   to leak out over the entire Inboard Zone of the Southern Alps (Fig. 4). Incursion of large

453   volumes of meteoric fluid into continental scale fault zones has been recorded elsewhere by

454   meteoric-like isotopic signatures of alteration minerals in the San Andreas fault zone (O'Neil,

455   1984) and indicates that deeply-sourced high pressure fluids from the mantle or dehydration

456   reactions need not be required to elevate pore fluid pressures in fault zones (Sleep and Blanpied,

457   1992).

4.4. Implications

459   High pressure fluids in fault zones have commonly been invoked to explain apparent

460   fault weakness in studies of continental-scale fault zones. We show that a large flux of meteoric

461   water passes through a limited rock volume in the hangingwall damage zone of the Alpine

462   Fault, above the low permeability PSZ fault "seal" that extends throughout the seismogenic

463   crust to ~8 km depth. Models predict a fluid flux of 10^{-2}-10^{-1} m^3/m^2/yr may be needed to

464   maintain high pore fluid pressures at 15 km depth in near-vertical fault zones with low cross-

465   fault permeability and at least three orders of magnitude permeability anisotropy (Faulkner and

466   Rutter, 2001). Our estimates for the flux of water through the Alpine Fault zone are within this

467   range (4×10^{-2} - 8×10^{-1} m^3/m^2/yr), indicating enough water may flow through the Alpine Fault

468   zone such that high pore fluid pressures could be generated which may contribute to fault

469   weakening and episodic fault rupture.

470   In addition, the presence of these fluids may impact on fault weakening by promoting

471   retrogression of primary minerals to weaker phyllosilicate minerals through fluid-rock

472   interactions in the damage zone of the fault. Fluid pressures in this region may be elevated

473   when secondary minerals precipitate and infill fractures, isolating fluids in high pressure

474   pockets within the damage zone (Blanpied et al., 1992; Byerlee, 1993), so-called pressure

475   compartmentalisation (Fulton and Saffer, 2009) and creep compaction may lead to the

476   development of pore fluid overpressures in the fault core (Sleep and Blanpied, 1992). These

477   processes may weaken the fault by reducing the effective normal stress, facilitating slip at low

478   shear stress (Rice, 1992).

479   Our strontium isotope data indicating fluid flow paths are restricted to the Alpine

480   Fault's hangingwall suggests that the cross-fault fluid flow barrier measured in shallow

481   boreholes extends throughout the seismogenic crust. If such a low permeability material

482   extends throughout the seismogenic crust it may affect earthquake rupture nucleation processes

483   by facilitating thermal pressurisation and dynamic weakening (Carpenter et al., 2014).

484   **5. Summary**

485   We present the first fully integrated fluid budget for a major continental fault, the Alpine

486   Fault (Fig. 4), using geochemical constraints on fluid sources, fluxes and flow paths (^{3}He/^{4}He,

487   δD, δ^{18}O, δ^{13}C, ^{87}Sr/^{86}Sr). We show that:

1. The Alpine Fault is a crustal-scale fault zone and acts as conduit for fluids from the mantle to the near surface. Clay and carbonate alteration in the Alpine Fault damage zone indicates a large flux of water and CO_2 has travelled through this zone and mantle $^3He/^4He$ ratios in warm springs near to the fault indicate the Alpine Fault is a conduit for a small flux of mantle fluids through the crust.

2. Strontium isotope analyses of warm springs and hydrothermal vein minerals indicate fluid flow is restricted to the hangingwall of the Alpine Fault and the fault acts as a barrier to cross-fault fluid flow throughout the seismogenic crust to ~8 km depth.

3. We identify fluid sources and independently calculate fluid fluxes from these sources in the Alpine Fault zone using $^3He/^4He$ ratios in warm springs and previously published stable isotope analyses of hydrothermal vein minerals. We calculate mantle H_2O and CO_2 fluxes of 2.5 to 12.6 mol/m^2/yr (4.5 x 10^{-5} to 2.3x10^{-4} m^3 STP m^{-2}/yr) and 0.2 mol/m^2/yr (4 x 10^{-3} m^3 STP m^{-2}/yr) respectively; a metamorphic H_2O flux of ~4 mol/m^2/yr (~7 x 10^{-5} m^3 STP m^{-2}/yr) distributed over the Inboard Zone of the Southern Alps and a maximum of 750 mol/m^2/yr focussed up a 100 m wide fault zone; and a meteoric H_2O flux of 2×10^3 to 4×10^3 mol/m^2/yr (4 x 10^{-2} to 8 x 10^{-2} m^3 STP /m^2/yr) up to 2×10^4 to 4×10^4 mol/m^2/yr (4 x 10^{-1} to 8 x 10^{-1} m^3 STP /m^2/yr)) focussed up a 100 to 1000 m wide fault zone. Meteoric water dominates and constitutes >99% of the fluid channelled up the Alpine Fault zone.

4. Geochemical tracer transport modelling suggests only ~0.02 to 0.05% of total rainfall west of the Main Divide penetrates to the top of the brittle to ductile transition zone at 6 km depth, yet this recharge flux is sufficient to overwhelm other fluid contributions.

5. Focussed fluid flow through the Alpine Fault zone may promote fault weakening by facilitating the formation of weak secondary minerals and promoting the generation of high pore fluid pressures or pressure compartmentalisation.

References

Adams, C.J., 2004. Rb-Sr and strontium isotopic characteristics of the Greenland Group, Buller
Terrane, New Zealand, and correlations at the East Gondwanaland margin. New Zealand Journal of
Geology and Geophysics 47, 189-200.

Adams, C.J., Campbell, H.J., Griffin, W.L., 2009. Tracing the Caples Terrane through New Zealand
using detrital zircon age patterns and radiogenic isotope signatures. New Zealand Journal of Geology
and Geophysics 52, 223-245.

Adams, C.J., Graham, I.J., 1997. Age of metamorphism of Otago Schist in eastern Otago and
determination of protoliths from initial strontium isotope characteristics. New Zealand Journal of
Geology and Geophysics 40, 275-286.

Barnes, I., Downes, C.J., Hurlston, J.R., 1978. Warm Springs, South Island New Zealand and their
potentials to yield Laumontite. American Journal of Science 278, 1412-1427.

Berryman, K.R., Cochran, U.A., Clark, K.J., Biasi, G.P., Langridge, R.M., Villamor, P., 2012. Major
Earthquakes Occur Regularly on an Isolated Plate Boundary Fault. Science 336, 1690-1693.

Bickle, M.J., McKenzie, D., 1987. The Transport of Heat and Matter by Fluids During Metamorphism.
Contributions to Mineralogy and Petrology 95, 384-392.

Blanpied, M.L., Lockner, D.A., Byerlee, J.D., 1992. An earthquake mechanism based on rapid sealing
of faults. Nature 358, 574-576.

Boese, C.M., Townend, J., Smith, E., Stern, T., 2012. Microseismicity and stress in the vicinity of the
Alpine Fault, central Southern Alps, New Zealand. Journal of Geophysical Research: Solid Earth 117,
B02302.

Boulton, C., Carpenter, B.M., Toy, V., Marone, C., 2012. Physical properties of surface outcrop
cataclastic fault rocks, Alpine Fault, New Zealand. Geochem. Geophys. Geosyst. 13, Q01018.

Byerlee, J., 1993. Model for episodic flow of high-pressure water in fault zones before earthquakes.
Geology 21, 303-306.

Carpenter, B.M., Kitajima, H., Sutherland, R., Townend, J., Toy, V.G., Saffer, D.M., 2014. Hydraulic
and acoustic properties of the active Alpine Fault, New Zealand: Laboratory measurements on DFDP-
1 drill core. Earth and Planetary Science Letters 390, 45-51.

Cox, S.C., Menzies, C.D., Sutherland, R., Denys, P.H., Chamberlain, C., Teagle, D.A.H., 2015. Changes
in hot spring temperature and hydrogeology of the Alpine Fault hanging wall, New Zealand, induced
by distal South Island earthquakes. Geofluids 15, 216-239.

Cox, S.C., Sutherland, R., 2007. Regional Geological Framework of South Island, New Zealand, and its
significance for Understanding the Active Plate Boundary, Continent-Continent Collision at the
Pacific/Indo Austalian Plate Boundary: Boundary, Motivation and Principal Results. American
Geolphysical Union, Washington DC, pp. 19-46.

de Leeuw, G.A.M., Hilton, D.R., Güleç, N., Mutlu, H., 2010. Regional and temporal variations in CO2/3He, 3He/4He and δ13C along the North Anatolian Fault Zone, Turkey. Appl. Geochem. 25, 524-539.

Faulkner, D.R., Rutter, E.H., 2001. Can the maintenance of overpressured fluids in large strike-slip fault zones explain their apparent weakness? Geology 29, 503-506.

Fulton, P.M., Saffer, D.M., 2009. Potential role of mantle-derived fluids in weakening the San Andreas Fault. Journal of Geophysical Research: Solid Earth 114, B07408.

Fulton, P.M., Saffer, D.M., Bekins, B.A., 2009. A critical evaluation of crustal dehydration as the cause of an overpressured and weak San Andreas Fault. Earth and Planetary Science Letters 284, 447-454.

Giggenbach, W.F., Sano, Y., Wakita, H., 1993. Isotopic composition of helium, and CO2 and CH4 contents in gases produced along the New Zealand part of a convergent plate boundary. Geochimica et Cosmochimica Acta 57, 3427-3455.

Harris, M., Coggon, R.M., Smith-Duque, C.E., Cooper, M.J., Milton, J.A., Teagle, D.A.H., 2015. Channelling of hydrothermal fluids during the accretion and evolution of the upper oceanic crust: Sr isotope evidence from ODP Hole 1256D. Earth and Planetary Science Letters 416, 56-66.

Hilton, D.R., Porcelli, D., 2003. Noble Gases as Mantle Tracers, in: Turekian, H.D., Holland, K.K. (Eds.), Treatise on Geochemistry. Pergamon, Oxford, pp. 277-318.

Horton, T.W., Blum, J.D., Craw, D., Koons, P.O., Chamberlain, C.P., 2003. Oxygen, carbon, and strontium isotopic constraints on timing and sources of crustal fluids in an active orogen: South Island, New Zealand. New Zealand Journal of Geology and Geophysics 46, 457-471.

Jenkin, G.R.T., Craw, D., Fallick, A.E., 1994. Stable isotopic and fluid inclusion evidence for meteoric fluid penetration into an active mountain belt: Alpine Schist, New Zealand. Journal of Metamorphic Geology 12, 429-444.

Jiracek, G.R., Gonzalez, V.M., Caldwell, T.G., Wannamaker, P.E., Kilb, D., 2007. Seismogenic, Electrically Conductive, and Fluid Zones at Continental Plate Boundaries in New Zealand, Himalaya, and California, USA, in: Okaya, D., Stern, T., Davey, F. (Eds.), A continental plate boudary: tectonics at South Island, New Zealand. American Geophysical Union, Washington DC, pp. 347-369.

Kennedy, B.M., Kharaka, Y.K., Evans, W.C., Ellwood, A., DePaolo, D.J., Thordsen, J., Ambats, G., Mariner, R.H., 1997. Mantle Fluids in the San Andreas Fault System, California. Science 278, 1278-1281.

Klemperer, S.L., Kennedy, B.M., Sastry, S.R., Makovsky, Y., Harinarayana, T., Leech, M.L., 2013. Mantle fluids in the Karakoram fault: Helium isotope evidence. Earth and Planetary Science Letters 366, 59-70.

Koons, P.O., 1987. Some thermal and mechanical consequences of rapid uplift: an example from the Southern Alps, New Zealand. Earth and Planetary Science Letters 89, 307-319.

Koons, P.O., 1990. Two-sided orogen: Collision and erosion from the sandbox to the Southern Alps, New Zealand. Geology 18, 679-682.

Kulongoski, J.T., Hilton, D.R., Barry, P.H., Esser, B.K., Hillegonds, D., Belitz, K., 2013. Volatile fluxes through the Big Bend section of the San Andreas Fault, California: Helium and carbon-dioxide systematics. Chemical Geology 339, 92-102.

Lamb, S., Smith, E., Stern, T., Warren-Smith, E., 2015. Continent-scale strike-slip on a low-angle fault beneath New Zealand's Southern Alps: Implications for crustal thickening in oblique collision zones. Geochemistry, Geophysics, Geosystems 16, 3076-3096.

Lockner, D., Tanaka, H., Ito, H., Ikeda, R., Omura, K., Naka, H., 2009. Geometry of the Nojima Fault at Nojima-Hirabayashi, Japan - I. A Simple Damage Structure Inferred from Borehole Core Permeability. Pure and Applied Geophysics 166, 1649-1667.

Manning, C.E., Ingebritsen, S.E., 1999. Permeability of the continental crust: Implications of geothermal data and metamorphic systems. Rev. Geophys. 37, 127-150.

Marty, B., Jambon, A., 1987. C/3He in volatile fluxes from the solid Earth: implications for carbon geodynamics. Earth and Planetary Science Letters 83, 16-26.

610   Menzies, C.D., Teagle, D.A.H., Craw, D., Cox, S.C., Boyce, A.J., Barrie, C.D., Roberts, S., 2014. Incursion
611   of meteoric waters into the ductile regime in an active orogen. Earth and Planetary Science Letters
612   399, 1-13.
613   Niedermann, S., Bach, W., Erzinger, J., 1997. Noble gas evidence for a lower mantle component in
614   MORBs from the southern East Pacific Rise: Decoupling of helium and neon isotope systematics.
615   Geochimica et Cosmochimica Acta 61, 2697-2715.
616   Norris, R.J., Cooper, A.F., 2007. The Alpine Fault, New Zealand: Surface Geology and Field Relations,
617   in: Okaya, D., Stern, T., Davey, F. (Eds.), A Continental Plate Boundary: Tectonics at South Island, New
618   Zealand. American Geophysical Union, Washington DC, pp. 157-175.
619   O'Neil, J., 1984. Water-rock interactions in fault gouge. pure and applied geophysics 122, 440-446.
620   Pickett, D.A., Wasserburg, G.J., 1989. Neodymium and strontium isotopic characteristics of New
621   Zealand granitoids and related rocks. Contributions to Mineralogy and Petrology 103, 131-142.
622   Pitcairn, I.K., Craw, D., Teagle, D.A.H., 2014. The gold conveyor belt: Large-scale gold mobility in an
623   active orogen. Ore Geology Reviews 62, 129-142.
624   Rice, J.R., 1992. Chapter 20 Fault Stress States, Pore Pressure Distributions, and the Weakness of the
625   San Andreas Fault, in: Brian, E., Teng-fong, W. (Eds.), International Geophysics. Academic Press, pp.
626   475-503.
627   Schleicher, A.M., Sutherland, R., Townend, J., Toy, V.G., van der Pluijm, B.A., 2015. Clay mineral
628   formation and fabric development in the DFDP-1B borehole, central Alpine Fault, New Zealand. New
629   Zealand Journal of Geology and Geophysics 58, 13-21.
630   Sibson, R.H., 1992. Implications of fault-valve behaviour for rupture nucleation and recurrence.
631   Tectonophysics 211, 283-293.
632   Sims, A., Cox, S.C., Fitzsimons, S.J., Holland, P., 2015. Seasonal infiltration and groundwater
633   movement in schist bedrock, Southern Alps, New Zealand. Journal of Hydrology (New Zealand) 54,
634   33-52.
635   Sleep, N.H., Blanpied, M.L., 1992. Creep, compaction and the weak rheology of major faults. Nature
636   359, 687-692.
637   Sutherland, R., Eberhart-Phillips, D., Harris, R.A., Stern, T., Beavan, J., Ellis, S., Henrys, S., Cox, S.,
638   Norris, R.J., Berryman, J.R., Townend, J., Bannister, S., Pettinga, J., Leitner, B., Little, T., Cooper, A.F.,
639   Yetton, M., Stirling, M., 2007. Do great earthquakes occur on the Alpine Fault in central South Island,
640   New Zealand?, in: Okaya, D., Stern, T., Davey, F. (Eds.), A Continental Plate Boundary: Tectonics at
641   South Island, New Zealand. American Geophysical Union Washington DC, pp. 235-251.
642   Sutherland, R., Toy, V.G., Townend, J., Cox, S.C., Eccles, J.D., Faulkner, D.R., Prior, D.J., Norris, R.J.,
643   Mariani, E., Boulton, C., Carpenter, B.M., Menzies, C.D., Little, T.A., Hasting, M., De Pascale, G.P.,
644   Langridge, R.M., Scott, H.R., Reid-Lindroos, Z., Fleming, B., Kopf, A.J., 2012. Drilling reveals fluid
645   control on architecture and rupture of the Alpine Fault, New Zealand. Geology 40, 1143 - 1146.
646   Toy, V.G., Boulton, C.J., Sutherland, R., Townend, J., Norris, R.J., Little, T.A., Prior, D.J., Mariani, E.,
647   Faulkner, D., Menzies, C.D., Scott, H., Carpenter, B.M., 2015. Fault rock lithologies and architecture
648   of the central Alpine fault, New Zealand, revealed by DFDP-1 drilling. Lithosphere 7, 206.
649   Tulloch, A.J., Ramezani, J., Kimbrough, D.L., Faure, K., Allibone, A.H., 2009. U-Pb geochronology of
650   mid-Paleozoic plutonism in western New Zealand: Implications for S-type granite generation and
651   growth of the east Gondwana margin. GSA Bulletin 121, 1236-1261.
652   Van Avendonk, H.J.A., Holbrook, W.S., Okaya, D., Austin, J.K., Davey, F., Stern, T., 2004. Continental
653   crust under compression: A seismic refraction study of South Island Geophysical Transect I, South
654   Island, New Zealand. Journal of Geophysical Research 109, B06302.
655   Wannamaker, P.E., Jiracek, G.R., Stodt, J.A., Caldwell, T.G., Gonzalez, V.M., McKnight, J.D., Porter,
656   A.D., 2002. Fluid generation and pathways beneath an active compressional orogen, the New
657   Zealand Southern Alps, inferred from magnetotelluric data. Journal of Geophysical Research 107,
658   ETG 6-1–ETG 6-20.
659   Warr, L.N., Cox, S.C., 2001. Clay mineral transformations and weakening mechanisms along the
660   Alpine Fault, New Zealand. Geological Society (London) Special Publication 186, 85-101.

⁸⁷Sr/⁸⁶Sr			
	range	average ± 1σ	n	Ref.
Hangingwall Alpine Schist	0.70391-0.71366	0.70911 ± 0.00190	45	1,2,3, new data current study
Footwall Palaeozoic Metasediments	0.72394-1.00182	0.78342 ± 0.05800	135	4,5,6
Footwall Granitoids	0.70846-0.77742	0.73538 ± 0.02600	11	5,6
Spring Waters	0.70843-0.71130	0.70935 ±0.00100	13 analyses of 8 springs	new data, current study
AFZ Hydrothermal Calcite	0.70405-0.71136	0.70794 ±0.00140	41	new data, current study

662 Table 1. Summary of strontium isotope data of host rocks either side of the fault, hangingwall

663 spring waters, and hydrothermal calcites from all depths. References: 1-Adams et al. (2009);

664 2-Adams and Graham (1997); 3-Horton et al. (2003); 4-Adams (2004); 5-Tulloch et al. (2009);

665 6-Pickett and Wasserburg (1989).

666

667

668

669

670

671

Calculation of the Mantle Fluid Flux		
<u>Measurements</u>	<u>Amythest Spring</u>	
Sample ^{3}He/^{4}He, R_s	0.81	R$_A$
Sample ^{3}He/^{4}He, absolute ratio	1x10^{-6}	
^{4}He concentration of sample, ^4He_s	3x 10^{-6}	cm^{3}STP/gH$_2$O
^{3}He concentration of sample	4x10^{-12}	cm^{3}STP/gH$_2$O
Mantle ^{3}He/^{4}He ratio, R_m	8	R$_A$
Mantle ^{3}He/^{4}He ratio, ^{3}He/^{4}He$_m$, absolute ratio	1x10^{-5}	
Original ^{4}He mantle concentration, $^4He_{fm}$	3x10^{-7}	cm^{3}STP/gH$_2$O
Crust ^{3}He/^{4}He ratio, Rc	0.02	R$_A$
U concentration in rock, U	3	ppm
Th concentration in rock, Th	13	ppm
<u>Constants</u>		

Porosity, $\varnothing$	0.1	kg/m/s
Crustal thickness, h_{crust}	35,000	m
Density rock, ρ_r	2700	kg/m^3
Density fluid, ρ_f	1000	kg/m^3
CO_2/^{3}He ratio mantle	2×10^9	
H_2O/^{3}He ratio mantle, min and max	3×10^{10}	1.4×10^{11}
^{4}He production rate, P^{4}He $\rho_r \times (1.19 \times 10^{-13} \times U + 2.88 \times 10^{-14} \times Th) \times (1-\varnothing)/\varnothing$	2×10^{-11}	cm^3/g/yr
^{3}He flow rate, q $(hc \times \rho_r \times PHe)/ (\rho f \times {}^4He_{fm}) \times (Rs - Rc)/(Rm-Rs)$	0.55	m/yr
^{3}He flux $q \times \rho_f \times {}^4He_s \times R_s$	2×10^{-10}	cm^{3}STP/cm^2/yr
	9×10^{-11}	mol/m^2/yr
Mantle Fluxes up the Alpine Fault		
Mantle H_2O flux maximum	12.6	mol/m^2/yr
Mantle H_2O flux minimum	2.5	mol/m^2/yr
Mantle CO_2 flux	0.18	mol/m^2/yr

672 Table 2. Calculation of the mantle fluid flux up the Alpine Fault following Kennedy et al.

673 (1997); Kulongoski et al. (2013) and using measured values from Amythest Spring (see Table

674 S4 for location details), which displays the highest ^{3}He/^{4}He ratio of all the springs measured

675 in this study.

676

677

Fluid Focussing Areas	All on narrow AFZ	All on wider AFZ	Imaged Conductive Zone	Inboard Zone
Width (m)	100	1000	2000	20000
Strike length (m)	1000	1000	1000	1000
Area (m^2)	10^5	10^6	2×10^6	2×10^7
Total Metamorphic (H_2O+CO_2) Output Flux (mol/m^2/yr)	750	75	38	**4**
Metamorphic CO_2 Output Flux (mol/m^2/yr)	**37.5**	**3.75**	1.9	0.2
Meteoric H_2O Output Flux (mol/m^2/yr)	**2×10^4 to 4×10^4**	**2×10^3 to 4×10^3**	1.2×10^3	120
Mantle H_2O Flux (mol/m^2/yr)		**2.5 to 12.7**		
Mantle CO_2 Flux		**0.2**		

(mol/m²/yr)

Table 3. Table outlining the different areas over which fluids may be focussed from depth. Shown are calculated output fluxes over these areas for metamorphic and meteoric fluids compared with the mantle fluid flux up the Alpine Fault crustal conduit.

Meteoric water time integrated flux calculation							
Variables							
Permeability, k, m²	1×10^{-15}	1×10^{-16}	$\mathbf{1\times10^{-17}}$	$\mathbf{1.5\times10^{-17}}$	$\mathbf{2.5\times10^{-17}}$	1×10^{-18}	
time, years	1,000	10,000	100,000	100,000	100,000	100,000	
relief, y, m	3000	3000	3000	3000	3000	3000	
length, x, m	20,000	20,000	20,000	20,000	20,000	20,000	
Hydraulic conductivity, K, m/s							
$(k \times \rho_f \times g) / \mu$	4.5×10^{-8}	4.5×10^{-9}	4.5×10^{-10}	6.8×10^{-10}	1.1×10^{-9}	4.5×10^{-11}	m/s
Darcy velocity, Q/A, volume/area/s							
$K \times (y/x)$	6.8×10^{-9}	6.8×10^{-10}	6.8×10^{-11}	1×10^{-10}	1.7×10^{-10}	6.8×10^{-12}	m³/m²/s
	2.1×10^{-1}	2.1×10^{-2}	2.1×10^{-3}	3.2×10^{-3}	5.3×10^{-3}	2.1×10^{-4}	m³/m²/y
Yearly input flux, volume/area/year							
$Q/A \times \rho_f$	1.9×10^{2}	1.9×10^{1}	$\mathbf{1.9\times10^{0}}$	$\mathbf{2.9\times10^{0}}$	$\mathbf{4.8\times10^{0}}$	1.9×10^{-1}	kg/m²/y
	1.1×10^{4}	1.1×10^{3}	$\mathbf{1.1\times10^{2}}$	$\mathbf{1.6\times10^{2}}$	$\mathbf{2.7\times10^{2}}$	1.1×10^{1}	mol/m²/yr
Time integrated flux, t, years							
$Q/A \times \rho_f \times t$	1.9×10^{5}	1.9×10^{5}	$\mathbf{1.9\times10^{5}}$	$\mathbf{2.9\times10^{5}}$	$\mathbf{4.8\times10^{5}}$	1.9×10^{4}	kg
	1.1×10^{7}	1.1×10^{7}	$\mathbf{1.1\times10^{7}}$	$\mathbf{1.6\times10^{7}}$	$\mathbf{2.7\times10^{7}}$	1.1×10^{6}	mol
Tracer transport distance, h							
O, $\Sigma flux/(\rho_s K_d/\rho_f)$ (<1 km)	*127*	*127*	*__127__*	*__190__*	*__317__*	*13*	m
H, $\Sigma flux/(\rho_s K_d/\rho_f)$ (>4 km)	*4177*	*4177*	*__4177__*	*__6265__*	*__10442__*	*418*	m

Table 4. Meteoric water time integrated fluid flux calculations tested by tracer transport distances. Highlighted in bold are variables that estimate fluid fluxes that are within range of tracer transport distances shown in Menzies et al. (2014).
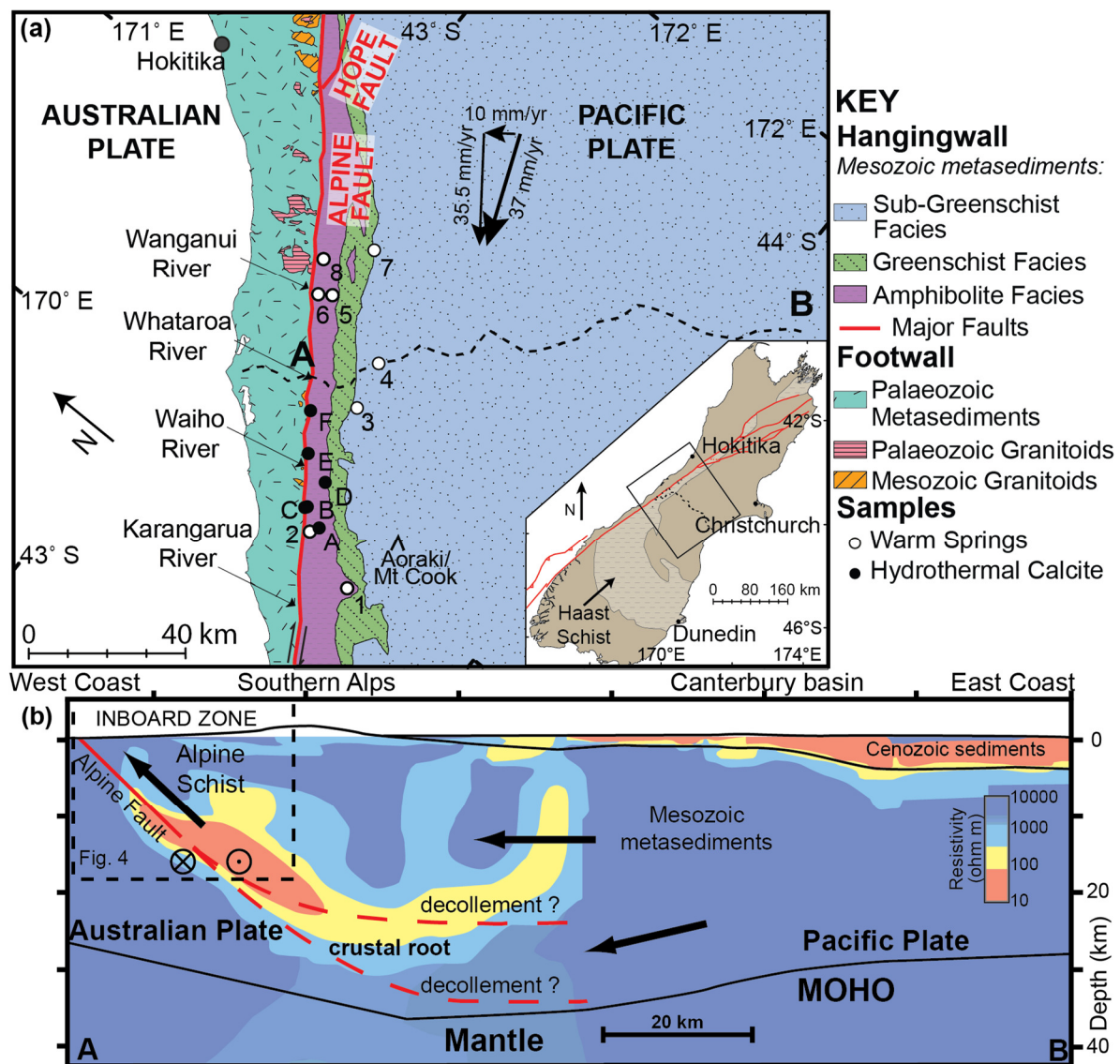
Fig. 1. (a) Geological map of South Island, New Zealand. Sample locations are outlined in the Supplementary data files Tables S3 and S4. Dashed line indicates resistivity cross-section AB. (b) Crustal-scale cross section incorporates fault model of Van Avendonk et al. (2004) and resistivity model from Jiracek et al. (2007). Dashed box signifies the area presented as Fig. 4.
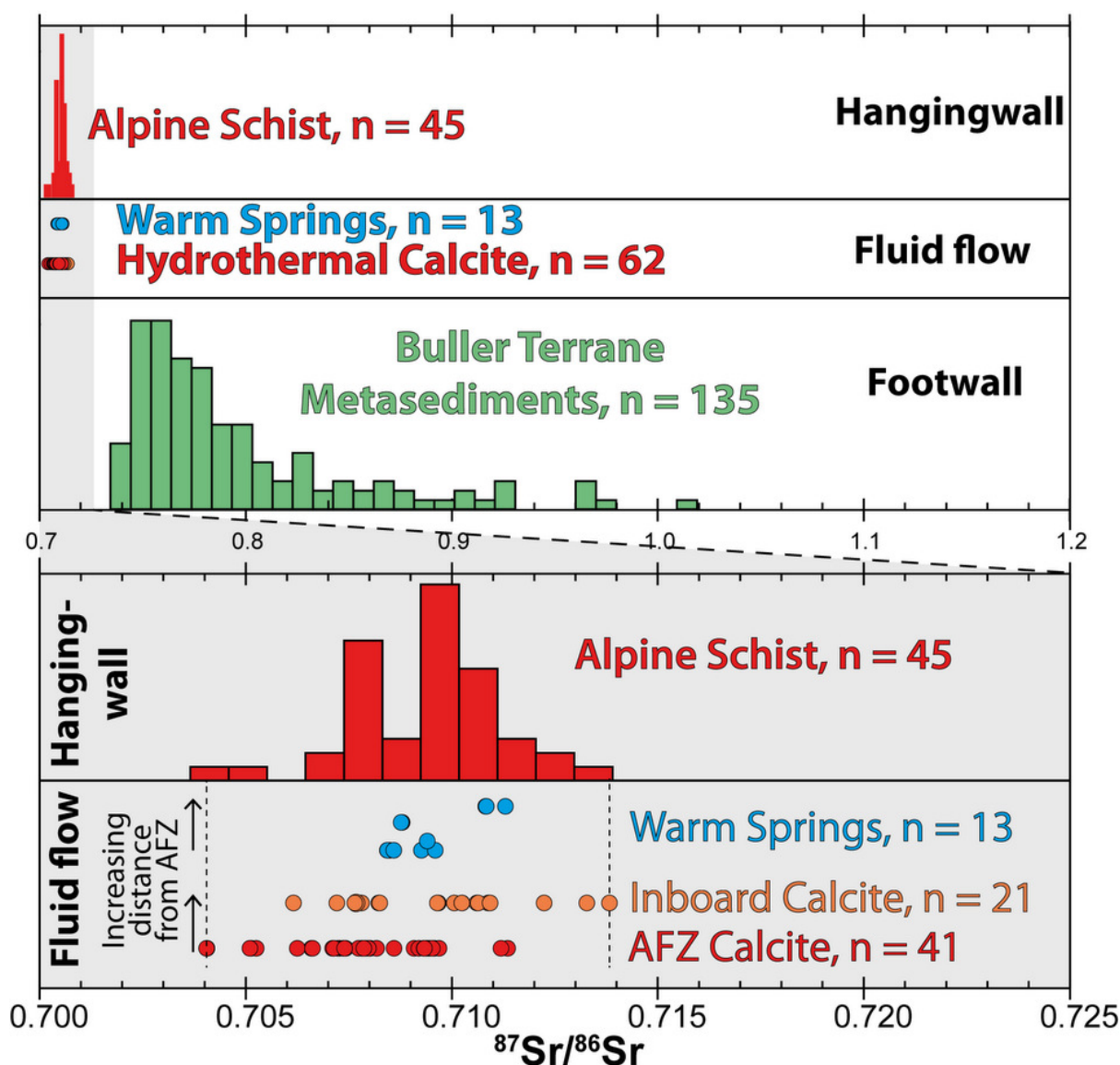
Fig. 2. The distributions of $^{87}Sr/^{86}Sr$ in footwall and hangingwall host rocks are compared with $^{87}Sr/^{86}Sr$ of hangingwall warm springs and hydrothermal minerals. Warm springs and hydrothermal minerals $^{87}Sr/^{86}Sr$ signatures are within range of hangingwall host rock Alpine Schist and do not appear to have obtained strontium from highly radiogenic footwall rocks. Footwall host rock data compiled from Adams (2004); Pickett and Wasserburg (1989); Tulloch et al. (2009) and hangingwall host rock data compiled from Adams et al. (2009), Adams and Graham (1997), Horton et al. (2003) along with new data collected in this study (see Table S6).
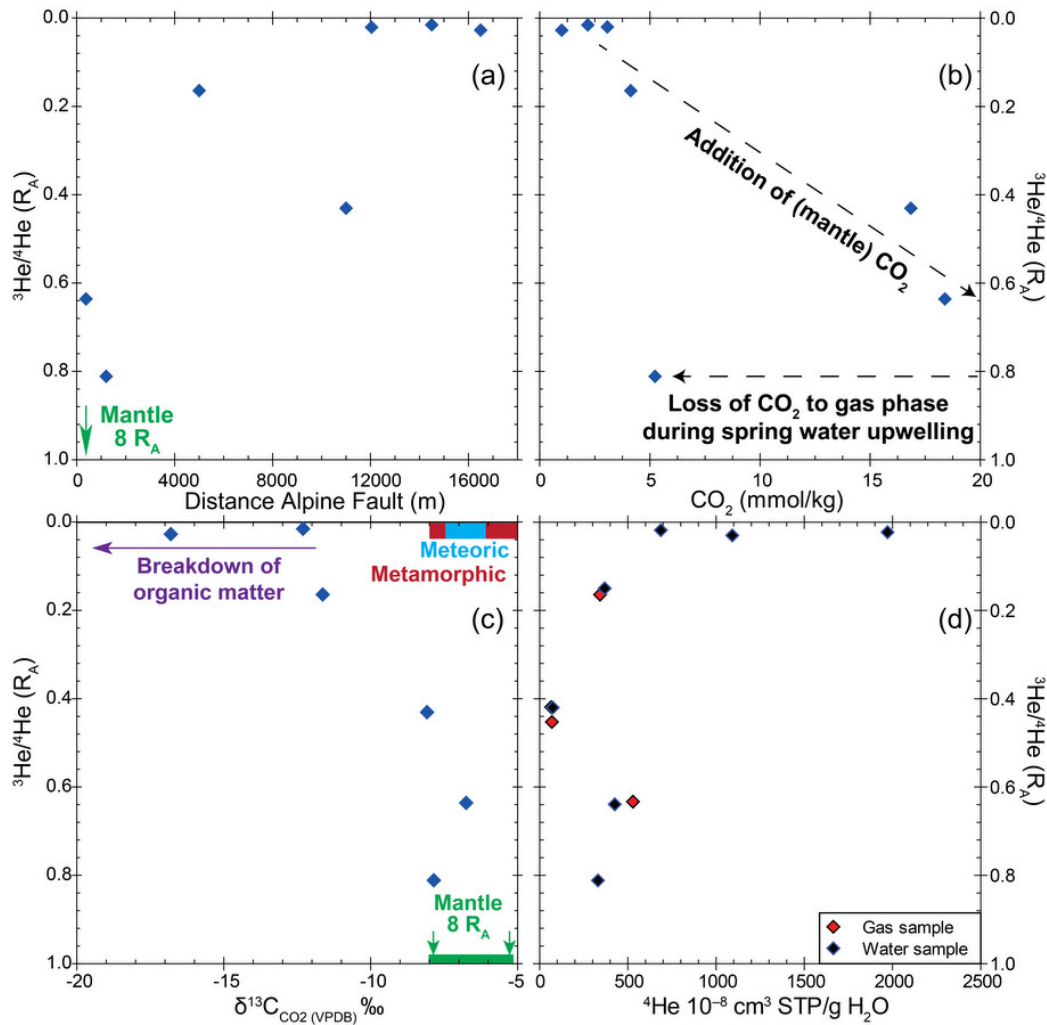
Fig. 3. (a) Air-corrected ^{3}He/^{4}He ratios versus distance southeast from the Alpine Fault. Springs closest to the Alpine Fault have a mantle helium contribution. (b) Air-corrected ^{3}He/^{4}He versus CO_2 concentrations in spring waters. Springs with elevated ^{3}He/^{4}He ratios distinctive of a mantle helium contribution have higher CO_2 concentrations than springs with only a crustal helium signature, indicating that the former have a contribution of mantle CO_2. Mantle ^{3}He/^{4}He value from Marty and Jambon (1987). (c) δ^{13}C values of warm spring waters that have a contribution of mantle He are higher than those with no mantle contribution. End member compositions from Jenkin et al. (1994) for carbon isotopes and for helium isotopes. (d) Total ^{4}He concentration versus ^{3}He/^{4}He ratio indicates that spring waters with no mantle contribution have the highest ^{4}He concentration and therefore the longest residence time.
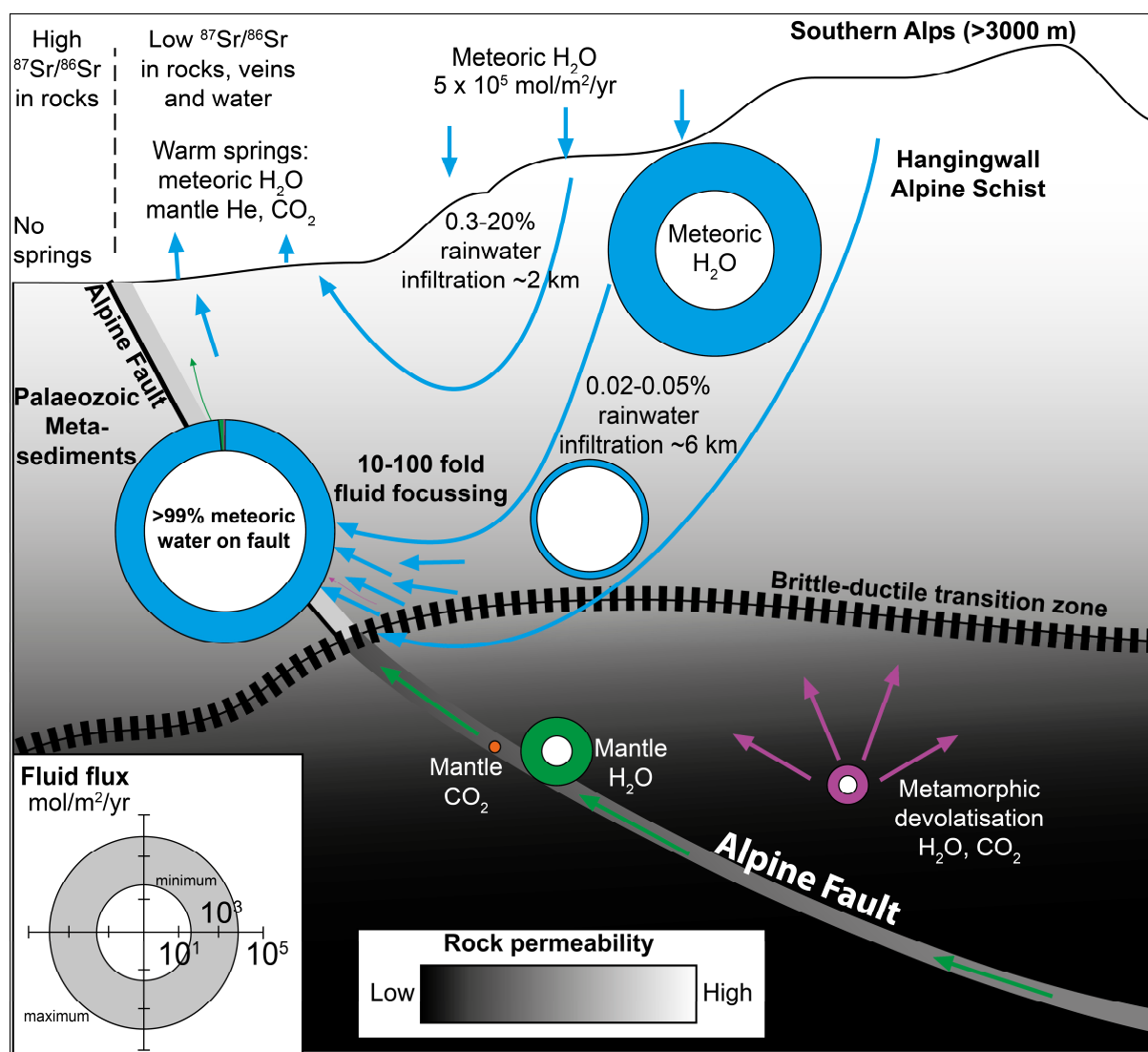
711

Fig. 4. Detailed view of the area of interest highlighted in Fig. 1b. Estimated fluxes of meteoric, metamorphic and mantle fluids are shown as coloured circles, with the inner and outer circles representing minimum and maximum estimates respectively. The proportion of each end member fluid that constitutes the flux up the Alpine Fault is illustrated as a proportional circle, meteoric water making up >99% of the total flux up the Alpine Fault. Initial rainwater infiltration ranges from Sims et al. (2015). Aspects of this figure are based on observations and data from quartz veins reported in Menzies et al. (2014).